Lattice simulations of phase morphology on lipid bilayers: Renormalization, membrane shape, and electrostatic dipole interactions

Jonathan J. Amazon* and Gerald W. Feigenson†
Field of Biophysics, Cornell University, Ithaca, New York 14850, USA
(Received 3 September 2013; revised manuscript received 2 December 2013; published 3 February 2014)

When liquid phases coexist at equilibrium but are not driven to minimize domain interfacial contact energy, the resulting patterns of phase domains can have important implications for living cells. In this study we explore some of the interactions and conditions that produce the stable patterned phases that are observed in model lipid mixtures. By use of Monte Carlo simulations we find that background curvature is important for the formation of patterned (modulated) phases. The interactions that stabilize nanoscopic phase separation are still not well understood. We show that inclusion of an electrostatic dipole repulsion with decay lengths as short as two to four lipid diameters can break up domains at the nanometer scale and that the location of the miscibility critical point is sensitive to this interaction. The use of a coarse-grained simulation raises questions about comparing parameters in simulations performed at different length scales. Using renormalization group techniques we show how to reconcile this problem, treating line tension as a running coupling constant.

DOI: 10.1103/PhysRevE.89.022702 PACS number(s): 87.16.aj, 87.16.af, 87.16.dt

I. INTRODUCTION

Lipid rafts are nanoscopic phase domains thought to exist in plasma membranes [1–4]. Rafts might be important for the cell to control protein localization, signaling, exocytosis, and endocytosis and have been implicated in virus assembly on the inner leaflet [5]. While the importance of lipid rafts is clear, the microscopic details of their formation and stability are still a question of active research.

The plasma membrane is composed of hundreds of individual lipid and protein species. To study the nature of lipid rafts, truncated model systems are employed that limit the complexity to just a handful of lipids. As few as three lipid species are sufficient to produce liquid-liquid ($L_d + L_o$) coexisting phases that are a visible manifestation of the domains postulated by the raft model of the plasma membrane [6–8]. Depending on the lipids used in model system studies, a wide range of phase morphologies can be realized. The system distearoylphosphatidylcholine (DSPC)–dioleoylphosphatidylcholine (DOPC)–cholesterol (chol) can exhibit macroscopic domains tens of microns in diameter, readily observable by optical fluorescence microscopy of giant unilamellar vesicles (GUVs) [9]. By contrast, the lipid system DSPC–palmitoyl,oleoyl-phosphatidylcholine (POPC)–chol appears uniform in GUV studies, but a large body of evidence, employing suboptical techniques such as Forster resonance energy transfer, electron spin resonance, and small-angle neutron scattering (SANS), supports the presence of coexisting phase domains at nanometer scales [10–13].

The nanodomains present in model systems are thought to be similar in nature to the lipid rafts of living cells [14,15]. Thus a thorough theoretical and empirical exploration of these model systems would clarify a fundamental biological phenomenon. To study the nature of this nanoscopic phase separation, we previously used a four-component lipid mixture to enable gradual composition-induced transition from GUVs exhibiting macroscopic phase domains (DSPC-DOPC-chol) to GUVs with nanodomains (DSPC-POPC-chol) [16,17]. This experiment revealed a narrow range of compositions that exhibits modulated phase behavior (patterned phases that are periodic and thermodynamically stable). Our previous study [18] found that modulated phases could be explained by a competing interactions model [19–21]: Line tension, which drives coexisting phases towards large round domains, competes against curvature energies, which penalize bending of the membrane.

This work expands the explorations of this model. We find that the line tension used to describe energy contributions from the phase boundary is highly sensitive to coarse graining. A renormalization group approach is used to formalize this problem and provide a workable solution. Renormalization was crucial for comparing simulations performed at different grain levels and for connecting our simulation results directly to experimental observations.

We also explore the role of background curvature in the stabilization of modulated phases on the surface of GUVs. Whereas all simulations in the previous study were performed on spherical lattices, which break the symmetry of the Hamiltonian and may facilitate patterning of the phases, here we construct lattices that lack this background curvature and compare the resultant morphologies for similar parameter sets.

With the success of a competing interaction model to explain modulated phases, we explore the use of electrostatic dipole repulsion between lipids as another potential interaction to compete with line tension to stabilize nanodomains. We study the effects of the dipole density in each phase and the decay length of the electric fields within the bilayer on phase morphology. Simulations are performed to study limited inclusion of curvature as an added degree of complexity. These results are compared directly to the domain size measurements of Heberle *et al.* [12] using SANS on 60-nm large unilamellar vesicles (LUVs).

*jja54@cornell.edu
†gwf3@cornell.edu

TABLE I. Default parameter set for studying effects of background curvature on modulated phase patterns.

Parameter	Value	Unit
u/kT	0.7	
κ_d,$-\bar{\kappa}_d$	10×10^{-19}	J
κ_o,$-\bar{\kappa}_o$	80×10^{-19}	J
P	0.5	
R	25	μm
kT	4.0×10^{-21}	J

II. MATERIALS AND METHODS

A. Monte Carlo simulation

We use a triangulated lattice to model the membrane and perform a Monte Carlo simulation to minimize a Hamiltonian defined on the vertices [18,22]. The perturbations explored at each step depend on the fields being studied. The Hamiltonian we had previously studied, the Helfrich energy functional [23], models the energetics of an elastic membrane S,

$$\mathcal{H}[S,\phi] = \gamma L + \iint_S \kappa(\phi)[H]^2 dA + \iint_S \bar{\kappa}(\phi) G\, dA, \qquad (1)$$

where γ is the line tension, L is the total length of phase boundary, κ is the bending modulus, and $\bar{\kappa}$ is the saddle-splay modulus. The parameters used in each section are defined in Tables I and II. The fields here are the phase field $\phi(\vec{r})$ (a binary field taking on the value 0 in the L_d phase and 1 in the L_o phase), the mean curvature field $H(\vec{r})$, and the Gaussian curvature field $G(\vec{r})$. To perturb the phase field ϕ, long-range exchanges are performed in which the phases of two randomly chosen vertices are exchanged. To perturb the curvature fields, a random vertex is moved a small distance (0.1% of the vesicle radius) in a random direction [22]. These two procedures enable the simulation to explore a large range of phase morphologies and vesicle shape deformations. Accepting or rejecting these perturbations using the Metropolis-Hastings criterion, with probability $P = e^{-\Delta E/kT}$, biases the simulation towards a minimal energy configuration, but still allows for entropic fluctuations.

Some key shape constraints prevent the surface from becoming nonphysical. Edge lengths are constrained so that each edge is free to fluctuate within $\pm 30\%$ of a specified value (here we use the average of the initial edge lengths). This keeps the lattice from self-intersecting while still allowing a reasonable degree of flexibility. The global area of the lattice is also harmonically constrained so that the total area of the membrane fluctuates by less than 1%. This constraint reflects the relatively high compression modulus of the membrane and keeps area fluctuations small. The simulation framework outlined above is exactly the same as in our previous work [18]. The changes introduced below are new to this study and extend the applicability of the simulation to more general cases.

TABLE II. Default parameter set for studying electrostatic effects on morphology.

Parameter	Value	Unit
u/kT	0.7	
μ_d	133	e^-/μm
μ_o	309	e^-/μm
k^{-1}	2	nm
κ_d,$-\bar{\kappa}_d$	2×10^{-19}	J
κ_o,$-\bar{\kappa}_o$	$\{8,14,20\} \times 10^{-19}$	J
R	30	nm
P	0.5	

B. Open surfaces and flat topology

The surface representation was changed to facilitate open surfaces and edges. This enables study of the behavior of flat open sheets of membrane and comparison of their behavior to that of curved membranes. An open surface can be modeled as a closed surface in which a subset of the vertices has missing neighbors. In the previous formalism we imposed the restriction that the array of neighbors for every vertex must form a closed counterclockwise loop. Here we lift this constraint and represent the missing points as a special value, internally referred to as BREAK, in the neighbor array. An example of the neighbor array for a vertex on the edge of a surface is shown in Fig. 1. The occurrence of a break signals the simulation to use edge-case versions of the geometric update routines.

Constructing the flat lattice requires defining the positions and neighbor arrays of each vertex. For an $N \times N$ flat array the position of the ith vertex is

$$\vec{v}_i = \left\langle \frac{(i\%N)}{N} + \frac{\lfloor i/N \rfloor \%2}{2N} - \frac{1}{2}, \frac{\sqrt{3}}{2}\left(\frac{\lfloor i/N \rfloor}{N} - \frac{1}{2}\right), 0 \right\rangle, \qquad (2)$$

where $\cdot\%\cdot$ is the modulo function and $\lfloor\cdot\rfloor$ is the floor function. This produces the triangular lattice grid shown in Fig. 2. The connectivity of this lattice is defined by the edges shown, with BREAK flags inserted where appropriate. The boundary conditions for the open surface hold the vertices at the edges fixed in space. This constraint keeps the surface from folding into itself, which was observed when the boundary points were allowed to move.

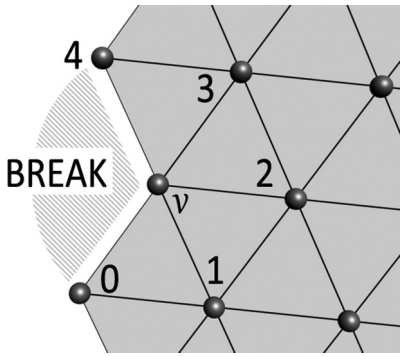

FIG. 1. Example of a vertex at the open edge of a surface. The neighbor array of v would read [0,1,2,3,4,BREAK]. The BREAK flag instructs the simulation to use special routines for calculating curvature, area, etc., at v.

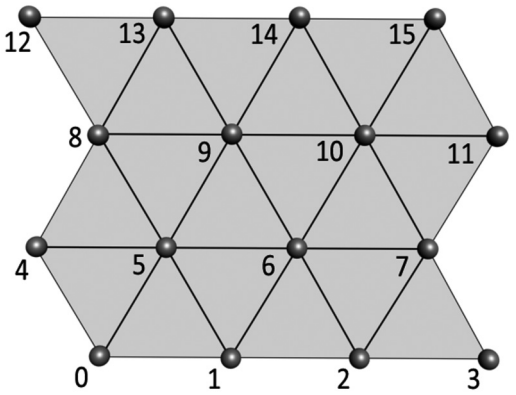

FIG. 2. A 4 × 4 flat lattice constructed using Eq. (2). Indexing runs from bottom left to top right with offsets on alternating rows to produce a triangular lattice.

C. Gaussian curvature on open surfaces

The inclusion of open surfaces requires a redefinition of the way Gaussian curvature is calculated on a discrete lattice. Gaussian curvature can be calculated by summing the angles between neighboring edges around a given vertex and subtracting this from 2π to determine the angle deficit [18,22]. This approach cannot be applied directly when the neighbors do not form a complete loop.

To generalize the computation of Gaussian curvature to vertices that could be adjacent to an edge, the fan formed by the faces around that vertex is projected onto the tangent plane at that vertex. The angle represented by the two edges adjacent to the break θ_P is then measured. This geometric construction is shown in Fig. 3. The equation for Gaussian curvature then becomes

$$G = \frac{(2\pi - \theta_P) - \sum \theta_i}{A}. \tag{3}$$

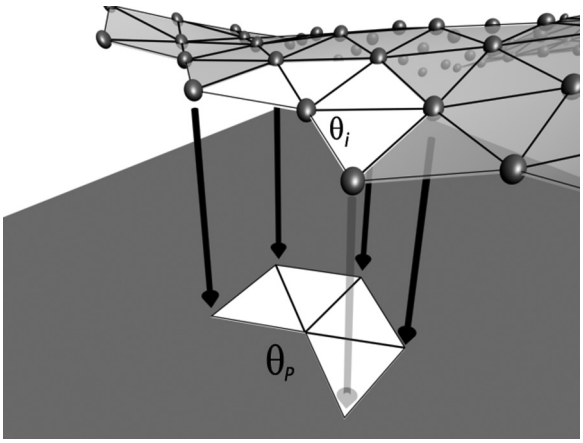

FIG. 3. Calculating Gaussian curvature at the surface edge. The fan around a given vertex is projected onto the tangent plane. The angle subtended by the gap in the projection is measured as θ_P. The angle deficit is then computed using $2\pi - \theta_P$ as the expected angle for zero curvature [Eq. (3)]. The angle θ_i is the angle between adjacent edges around the vertex (not including the break).

This procedure satisfies the Gauss-Bonnet theorem (see Ref. [24]) and produces a smoothly varying Gaussian curvature even at the edges of the surface.

D. Electrostatics model

Electrostatic interactions from permanent molecular dipoles of lipid moieties and bound water might be interactions that compete with line tension [25]. In the context of large (micron-size) phase domains, the effects of electrostatics can be largely ignored due to electrostatic screening. The electric fields within the bilayer have a decay length on the order of a few nanometers, caused by the salt in the surrounding medium and the symmetric geometry of the bilayer [17,26]. In the context of nanodomains, a few nanometers may represent several lipid shells, implying that electrostatic interactions cannot be ignored.

To model the electrostatics we define a dipole density at each vertex that depends only on the local phase,

$$\mu(v) = \begin{cases} \mu_d & \text{if } v \in L_d \\ \mu_o & \text{if } v \in L_o. \end{cases} \tag{4}$$

The electric field at each vertex is defined by summing over the remaining vertices of the lattice and adding up the contribution of each according to the following [19,25,27]:

$$\vec{E}(v) = \frac{1}{4\pi\epsilon} \sum_{x \neq v} e^{-k\|\vec{r}\|} \left[\frac{3(\vec{n}\cdot\vec{r})\vec{r}}{\|\vec{r}\|^5} - \frac{\vec{n}}{\|\vec{r}\|^3} \right] \mu(x) A(x), \tag{5}$$

where $\vec{n}$ is the membrane normal at x, $\vec{r}$ is the vector connecting v and x, k is the decay length of the fields within the membrane, and $A(x)$ is the area of vertex x. This equation has three important terms: The leading exponential function expresses the fact that the electric fields within the plane of the bilayer decay with a characteristic length that depends on the salt concentration of the surrounding medium and the thickness and geometry of the bilayer; the portion in large square brackets is the electric field contribution at v from a point dipole at position x (oriented normal to the membrane); the last term is the magnitude of this point dipole at position x. With this field defined, the energy functional becomes

$$\mathcal{H} = \gamma L - \sum_v 2\mu(v) A(v) \vec{n} \cdot \vec{E}(v). \tag{6}$$

A factor of 2 is needed to take into account that both leaflets of the membrane experience a mirrored electric field. The assumed geometry of the lipid dipoles in the membrane and the field lines that are produced by Eq. (5) are shown in Fig. 4. Notice that the dipole density is always assumed parallel to the membrane normal. We make this assumption because, whereas individual lipid dipole moments may orient away from the bilayer normal, the rotational symmetry of the liquid phase ensures that in-plane contributions to the dipole density will average to zero.

E. Quantifying morphology: Radial distribution function

To study how the various parameters and interactions affect the clustering of phase domains, we use the L_o-L_o radial distribution function, which gives the probability density of finding a vertex of L_o phase as a function of distance from

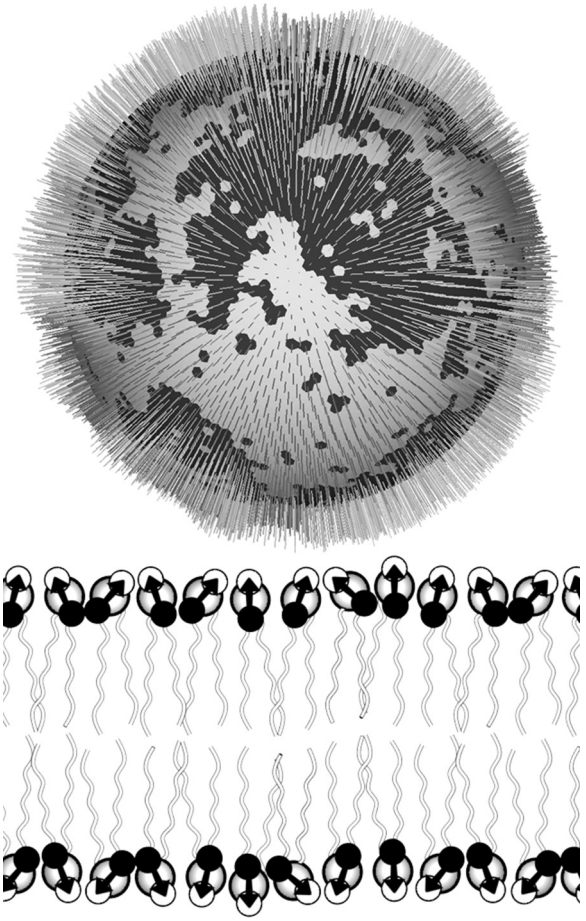

FIG. 4. The top shows electric field lines [as defined by Eq. (5)] on the surface of a simulated GUV. The bottom shows the microscopic geometry of the charge distribution assumed in the formulation of the electrostatics model. Black beads represent point positive charges, white beads point negative charges, and black arrows the net individual dipole moments of each lipid.

another vertex of L_o. To estimate this distribution we produce a histogram with bin width $\langle \Delta r \rangle$, defined as the average distance between neighboring vertices. We define the set $B_v(i)$ as all vertices in a spherical shell around the vertex v,[1]

$$B_v(i) = \{w | i\langle \Delta r\rangle < \|\vec{w} - \vec{v}\| < (i+1)\langle \Delta r\rangle\}, \qquad (7)$$

and let $N_v(i)$ be the number of elements in $B_v(i)$. The L_o-L_o correlation function can then be defined by counting the number of elements in each bin for each vertex and normalizing,

$$C(i\langle \Delta r\rangle) = \frac{1}{PN} \sum_{v \in L_o} \left[\frac{1}{N_v(i)} \sum_{w \in B_v(i)} \delta_{\phi_v \phi_w} \right], \qquad (8)$$

where δ is the Kronecker delta function, P is the area fraction of L_o phase, and N is the total number of vertices on the lattice. In this treatment distance between vertices is measured along the contours of the surface and C is defined only at discrete intervals set by the bin width $\langle \Delta r \rangle$.

[1]The symbol v refers to the scalar index of the vertex, while the symbol $\vec{v}$ refers to the vector position of the vertex in space.

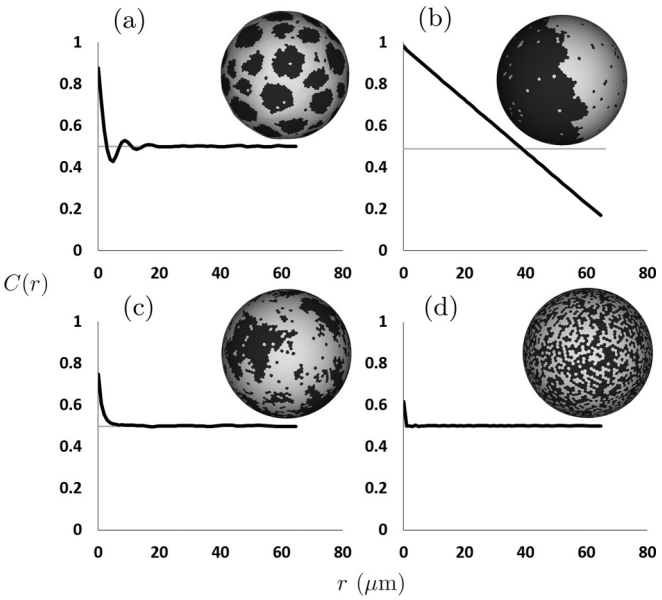

FIG. 5. Different morphologies give rise to distinct shapes of their correlation function, which measures the probability of finding like phases at a distance r from each other. (a) Modulated phases show damped oscillations corresponding to the repeat length of the patterns. (b) Macroscopic domains show a linear or sigmoidal decrease (see Fig. 10) that crosses the $C(r) = P$ axis at approximately the domain size. (c) Clusters and critical fluctuations show an exponential decay that defines a correlation length and (d) random mixing yields a straight horizontal line at $C(r) = P$. In the above examples, the area fraction $P = 0.5$.

The correlation function can be used to distinguish among the various morphology possibilities: random mixing, clustered domains, modulated phases, and macroscopic domains. These various morphologies are shown in Fig. 5. Random mixing yields a constant value of $C(r) = P$, clustered domains have an exponential decay that defines a correlation length, modulated phases show a distinct periodicity that defines the repeat length of the patterns, and macroscopic domains yield a roughly linear or sigmoidal correlation function that crosses the line $C(r) = P$ at the domain size.

F. Heat capacity

Heat capacity is useful to assess how competing interactions change the thermodynamic properties of the model. The heat capacity at constant volume can be defined as

$$h \propto \langle \mathcal{H}^2 \rangle - \langle \mathcal{H} \rangle^2. \qquad (9)$$

It is sufficient for our purposes to define a quantity that is proportional to the actual heat capacity because we are interested in the *locations* of features of the curve, such as peaks or discontinuities, rather than numerical values. Because heat capacity is a statistical measure, we must consider error and correlation in the measurements. Heat capacity was measured by taking 1000 samples of the total energy at intervals separated by $100 \times N$ Monte Carlo steps to minimize

autocorrelation. This process still produces curves with high variance, but the important features are readily visible.

III. RESULTS AND DISCUSSION

A. Line tension and renormalization

One useful feature of this coarse-grained simulation approach is its applicability to a wide range of size scales. By changing the size and resolution of the lattice one can simulate from 100-μm-diam GUVs, where each vertex represents hundreds of thousands of lipids, down to 0.06-μm-diam LUVs, where each vertex represents only a few lipids. In order to relate the simulation results to physical observations it is important to consider the problem of running coupling constants [28]. This is the tendency of certain parameters to change when degrees of freedom are lost in coarse graining.

This problem becomes apparent when comparing simulations with the same parameter set and changing only the resolution of the lattice. Parameters that give macroscopic phase separation at lower resolution (10 000 vertices) can yield random mixing on a higher resolution lattice (40 000 vertices). This is due to the line tension being a running coupling constant. In this section we consider a Hamiltonian that includes only the contribution from line tension $\mathcal{H} = \gamma L$ in order to determine how it changes under coarse graining. A bending modulus can be treated in a similar way [29]. To compare the line tension on different resolution lattices we define the scale-invariant quantity $u \equiv \gamma l_0$, where l_0 is the average boundary length contribution for a pair of adjacent vertices. This makes our model roughly equivalent to an edge-counting Ising model

$$\mathcal{H} = \sum_{\langle i,j \rangle} \frac{\gamma l_0}{2}(1 - S_i S_j) \tag{10}$$

$$= \sum_{\langle i,j \rangle} -\frac{u}{2} S_i S_j, \tag{11}$$

where $S_x = 2\phi_x - 1$ and we have discarded the constant energy offset. In this form we can relate our simulation to the known solution of the Ising model on a triangular lattice [30]. Criticality for this system occurs when

$$\frac{u_{\text{crit}}}{kT} = \frac{\ln(3)}{2} \approx 0.55. \tag{12}$$

For u/kT below this critical value the lattice simulation should function exactly as a triangular lattice Ising model with zero external field. We can test this by measuring the heat capacity as a function of u/kT, shown in Fig. 6. The heat capacity curves $h(u/kT)$ for both the flat and spherical lattices show no remarkable differences and most importantly both show a sharp peak at $u/kT \approx 0.55$, consistent with the theoretical value for the critical point of the triangular lattice Ising model. This close match in critical point is surprising because the flat lattice has a valence of exactly 6, whereas the spherical lattice has many 5-7 defects and only an average valence of 6.

The next step is to formulate a means of relating the morphology on lattices at different grain levels. The grain level is defined as the number of lipids represented by each vertex $G \equiv a_v/a_0$, where a_0 is the area of a single lipid and

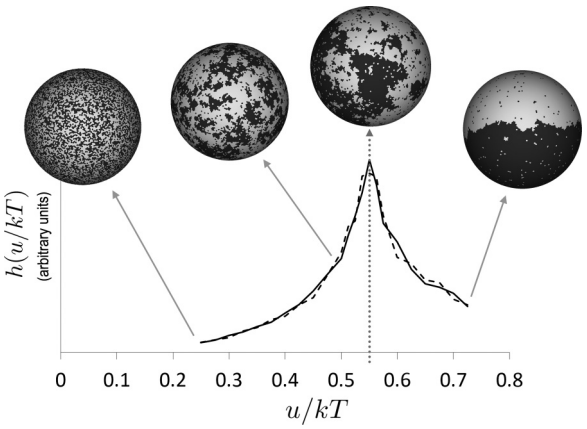

FIG. 6. Heat capacity as a function of line tension for both spherical (solid black line) and flat (dashed black line) lattices. The peak corresponds to $u/kT = 0.55 \approx \ln(3)/2$, the theoretical critical point of the triangular Ising model.

a_v is the average area of a single vertex. Two morphologies at different grain levels are defined to be equivalent if both have the same inverse correlation length, where the inverse correlation length is given by

$$c(u/kT) \equiv \left(-\frac{dC(r)}{dr}\bigg|_{r=0} \right) - c_{\text{crit}}. \tag{13}$$

Shifting this curve by the value of c_{crit} fixes the inverse correlation length at the critical point to be zero $[c(u_{\text{crit}}/kT) = 0]$, thus ensuring that the critical point is a fixed point under renormalization. The value c_{crit} is determined empirically through simulation.

The curves for $c(u/kT)$ at two different grain levels and an illustration of the renormalization procedure are shown in Fig. 7. Notice that $c(u/kT)$ need only be measured at a single grain level G_1, because changing the grain level to

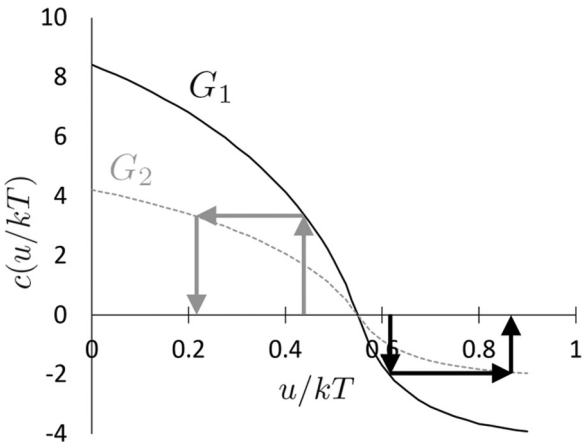

FIG. 7. Inverse correlation length relates line tension at two different grain levels G_1 (solid black line) and G_2 (dashed gray line). A value of u_1/kT is chosen for grain level G_1. The corresponding value for G_2 is determined and the value of u_2/kT is read off the axis. Values of u/kT below the critical point shift towards zero under coarse graining (gray arrows), whereas values above the critical point shift towards ∞ (black arrows).

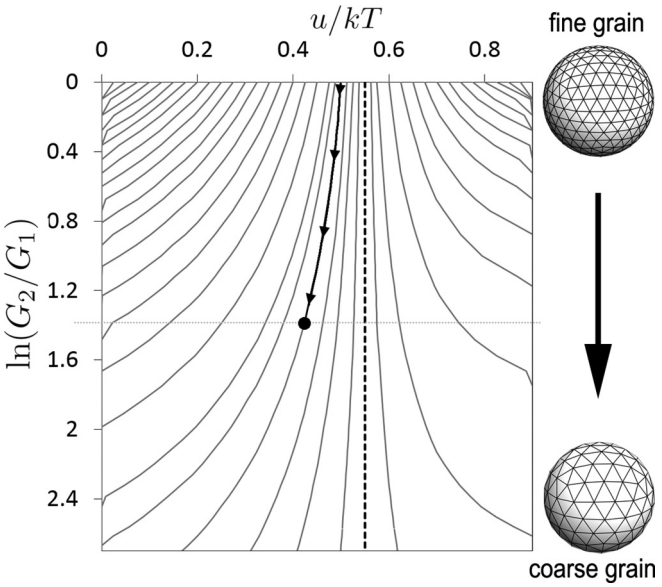

FIG. 8. Renormalization flows of u/kT going from a fine-grained simulation (top) to a coarse grained simulation (bottom). To relate u at two different grain levels, follow the contours from the top down to the appropriate value of $\ln(G_2/G_1)$. For example, coarse graining by a factor of $G_2/G_1 = 4$ [$\ln(G_2/G_1) = 1.39$, dotted gray line] with a line tension of $u_1/kT = 0.5$ (black line with arrows) gives a renormalized value of $u_2/kT = 0.425$. The critical manifold (dashed black line) remains fixed under renormalization.

G_2 only introduces a constant prefactor of $\sqrt{G_1/G_2}$. When coarse graining from grain level G_1 to G_2, the condition that the inverse correlation length remains fixed is given by the scaling relation

$$\frac{c(u_2/kT)}{\sqrt{G_2}} = \frac{c(u_1/kT)}{\sqrt{G_1}}. \tag{14}$$

For any given values of u_1, G_1, and G_2 this relation is numerically solved for u_2, giving rise to a set of renormalization flows as grain level G_2 increases. The flows are shown in Fig. 8. By following these flows we can relate the value of u from one grain level to another and hence make meaningful comparison of the resultant phase morphologies when other parameters (such as vesicle size) are varied.

The renormalization flows show several important aspects of the scaling behavior in the simulation. Below the critical point, u tends towards 0, indicating clusters of finite size, which will eventually be below the lattice resolution. At the critical point (black dashed line) renormalization does not change line tension because the morphology is fluctuating on all length scales in a self-similar way [31,32]. Above the critical line tension, u tends towards ∞. This is because underresolving the boundary of a large domain is equivalent to damping out its fluctuations, which shows up as an increase in line tension.

Figure 9 shows how this scaling procedure affects the morphology of lattices at different grain levels. As an example we illustrate a lattice of 40 000 vertices being coarse grained to a 10 000 vertex lattice (holding vesicle size fixed), giving a grain level of $G_2/G_1 = 4$. For naive coarse graining, where line tension is treated as a true energy per unit length, the morphologies can be radically different and comparison

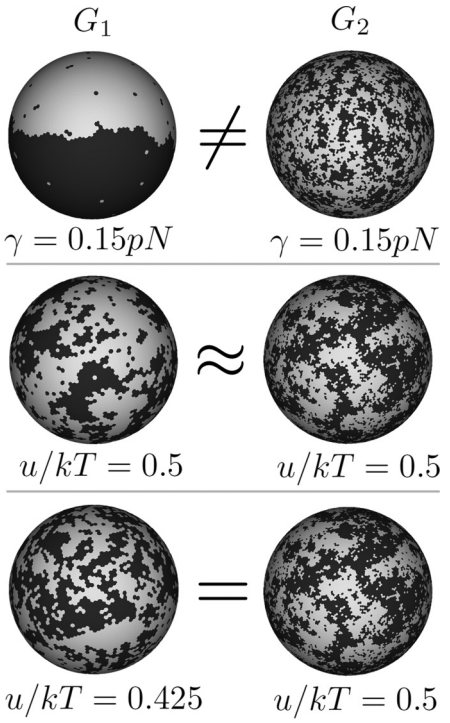

FIG. 9. Renormalization is required in order to compare simulations having different levels of coarse graining. The two lattices above have 10 000 vertices (left G_2) and 40 000 vertices (right G_1). Holding the true line tension fixed under coarse graining (top) leads to radically different morphologies. Holding the scaleless line tension fixed (middle) at $u_1/kT = u_2/kT = 0.5$ produces qualitatively similar morphology, but different correlation length. Using the renormalization flows (bottom), coarse graining by $G_2/G_1 = 4$ yields $u_2/kT = 0.425$. This produces equivalent morphologies with similar correlation length.

becomes meaningless. Using the scale-invariant form of line tension u for both grain levels $u_1/kT = u_2/kT = 0.5$, there is qualitative agreement between the morphologies, but the linear dimension of the structures is still off by a factor of $\sqrt{G_2/G_1}$. Using renormalization flows for $u_1/kT = 0.5$ and $G_2/G_1 = 4$, the value $u_2/kT = 0.425$ is used for the coarse-grained lattice (solid black line in Fig. 8). These values produce both qualitative agreement and structures of the same linear dimension.

This exercise in renormalization outlines the potential pitfalls of coarse graining a model when parameters that are sensitive to the removal of degrees of freedom may be present. We have also outlined a general procedure for empirically solving renormalization flows whenever an equivalence class can be defined that is independent of the grain level (in our case, phase morphologies with the same inverse correlation length).

B. Flat and spherical lattices

Previous simulations have shown that the competition between line tension and curvature energies, defined by the Helfrich energy functional (1), can stabilize modulated phases. These results closely match the characteristics of modulated phase patterns observed on GUVs in the four-component

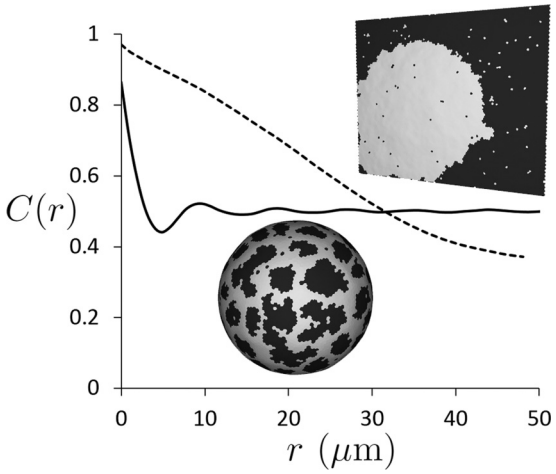

FIG. 10. With parameters that give rise to modulated phases (Table I) on a spherical lattice (solid curve), modulated phases do not appear on a flat lattice (dashed curve).

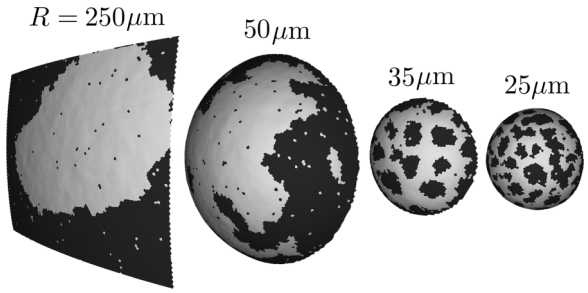

FIG. 11. Background curvature is important to stabilizing modulated phases. From right to left the background radius of curvature is increased. Each simulation shown has the same area per vertex (0.78 μm^2/vertex) and is drawn on the same absolute length scale for comparison.

lipid system DSPC/DOPC/POPC/chol. All of the previous simulations were performed on a triangulated spherical surface to best approximate the shape and size of the observed GUVs. The spherical lattice imposes a constant background curvature that breaks the symmetry of the energy functional and may play an important role in the formation of modulated phase patterns. To better understand the role that this symmetry-breaking plays in the formation of modulated phases we perform simulations on spherical and flat lattices to compare the resultant phase morphology.

1. *Modulated phases do not appear on flat lattices for parameters that produce modulated phases on spherical vesicles*

Simulations were performed with the parameters shown in Table I. The value of line tension $u/kT = 0.7$ ensures that the model is in the two-phase region, but is low enough so as not to dominate the energy landscape. The bending moduli are slightly higher than literature reported values [33], but are chosen to produce modulated phase patterns. Setting $\bar{\kappa} = -\kappa$ is consistent with literature estimates [34]. These parameters give modulated phases when used on a 50-μm-diam spherical surface. When these same parameters are used on a flat lattice with dimension 96×83 μm^2 (equal area and vertex density), modulated phases do not appear. Simulation correlation functions and the representative morphologies are shown in Fig. 10. This finding implicates background curvature as a stabilizing factor in curvature-induced modulated phases.

2. *Background curvature is important in stabilizing modulated phases*

To study how background curvature affects the formation and stability of modulated phases a series of simulations was performed in which only the background radius of curvature was changed. To produce different background curvatures the spherical and flat lattices were molded, scaled, and truncated to produce open spherical caps with the same vertex density. The observed changes in morphology are shown in Fig. 11. We find that for the parameter set explored, background curvature is necessary for the stability of patterns. Increasing the radius of curvature by about 50% (to 35 μm) causes a broadening of the domain size, while a doubling of the radius of curvature (50 μm) is sufficient to altogether arrest the formation of a well-defined periodic pattern. Macroscopic domains persist as the radius of curvature is further increased. The sudden onset of modulated phases as the surface is curved represents a buckling instability that exchanges the energy cost of bending a large L_o domain for an increase in phase boundary. Similar curvature-induced morphological instabilities have been observed that minimize the phase boundary using out-of-plane deformations of the membrane [35]. These observations may have implications for raft morphology, given the large variations in curvature observed for living cells [36].

C. Nanodomains and electrostatics

So far the simulation outlined successfully models GUVs with optically resolvable modulated phases and macroscopic domains. To study the nanoscopic phase separation observed in some model systems [1,13,21,37], the simulated vesicle is scaled down so that each vertex represents only a handful of lipids. At this scale nanometer-size domains are resolvable, allowing us to explore their morphology and stability. Here we simulate vesicles that are 60 nm in diameter with a resolution of 10 000 vertices, giving a grain level of approximately two lipids per vertex. Our motivation for this particular vesicle size is that 60-nm vesicles are used by Heberle *et al*. in small-angle neutron scattering to study the size and distribution of nanodomains [12].

When each vertex represents only a few lipids, it is necessary to consider electrostatic dipole interactions, which vary on this length scale. Previous calculations of the range of the electric fields within bilayers showed a decay length between 2 and 4 nm depending on the concentration of salt in the surrounding medium [17]. For GUV simulations of optical phenomena this allowed treating dipole interactions as a contribution to the mechanical parameters describing the Helfrich energy functional and enabled obtaining bending modulus values directly from experiment [33]. At the nanodomain scale this decay length represents several lipid shells and thus must be treated as a separate term in the energy functional as described by Eqs. (5) and (6). Since the microscopic origin

of the electrostatic interaction is approximated as adjacent, parallel molecular dipoles, it is necessarily a dispersive interaction that will compete with line tension. This provides a potential mechanism for the stabilization of nanoscopic phase separation.

1. Electrostatic parameters

To implement this model we start with approximate values for the electrostatic parameters. The key parameter that controls the magnitude of the interaction is the dipole density of each phase μ_d and μ_o. The most robust measurement of this parameter comes in the form of the dipole potential Ψ_d [38], which is the difference in electrostatic potential between the surface and interior of the membrane. This value is on the order of 300 mV for the L_d phase and has been estimated to be as high as 1000 mV for the L_o phase [39,40]. In order to convert such a measurement to dipole density we must assume a geometry for the charge distribution. The simplest geometry that captures the essential features of the transmembrane potential has the headgroups as a parallel plate capacitor. A positively charged plate is placed at the headgroup-chain interface and a negatively charged plate at the headgroup-water interface [25,27]. This provides the simple relation $\mu = \epsilon\Psi_d$ for the dipole density, where ϵ is the effective dielectric experienced by the molecular dipoles.

The dielectric constant ϵ for our simulation is not well determined. The electrostatic environment within the headgroup region of the membrane is very complicated. It has a high degree of anisotropy with estimates of the normal and lateral components of the dielectric tensor ranging over two orders of magnitude [41,42]. We constrain our value of ϵ by noting that the major contributions to the dipole density come from the carbonyl groups that link the acyl chains to the glycerol backbone and from bound water [43]. The zwitterionic phosphotidylcholine headgroup is oriented nearly parallel to the membrane surface and thus contributes little to the normal component of the dipole density [40]. With this in mind we choose $\epsilon = 8$ to emphasize that the carbonyls are partially submerged in the hydrocarbon portion of the bilayer, which has a low dielectric [27,38,41,44]. Using these values in the parallel plate capacitor equation yields an estimate for the L_d dipole density of $\mu_d = 133\ e^-/\mu$m. For the L_o phase we use the value $\Psi_d = 700$ mV [39], which gives a dipole density of $\mu_o = 309\ e^-/\mu$m. This contrast between the two phases $\Delta\mu = \mu_o - \mu_d = 176\ e^-/\mu$m produces the frustration that could drive the breakup of macroscopic domains.

The other parameter in Eq. (5) that needs to be addressed is the decay length of the electric fields within the plane of the bilayer k^{-1} (not to be confused with the Debye length in the aqueous surrounding medium). This parameter is well constrained and depends on the salt concentrations in the surrounding medium and the geometry of the bilayer. Previous simulations of the Debye-Hückel equation allowed solving for the electrostatic potential in and around a circular phase domain and enabled calculating this decay length [17]. See Ref. [24] for a detailed explanation of these calculations. We found the accessible range of decay lengths from $k^{-1} \approx 1$ nm at arbitrarily high salt concentrations up to $k^{-1} \approx 4$ nm for a surrounding medium of pure water. We used a default value $k^{-1} = 2$ nm, corresponding to a physiological concentration of salt in the surrounding medium.

In Secs. III C 2–III C 4 we consider only the competition of line tension and electrostatics as given by Eq. (6). In Sec. III C 5 we consider the added complexity of curvature in tandem with line tension and electrostatics. Line tension is chosen to be $u/kT = 0.7$ because this yields the two-phase region while still exhibiting interesting behavior with the electrostatic parameters derived above. We set the phase fraction of the membrane to be $P = 0.5$ to emulate being in the center of a tie line far from any phase boundaries in composition space. The default parameter set for our exploration of electrostatics is shown in Table II unless otherwise stated. The bending moduli shown only apply to Sec. III C 5, where Helfrich curvature terms are included.

2. Contrast in dipole density between phases breaks up phase domains

The contrast in dipole density between the two phases $\Delta\mu$ dictates the magnitude of the electric fields. To explore how the dipole interactions disrupt the phase domain morphology we examine the correlation functions for a series of simulations with $\Delta\mu = 0$ up to $\Delta\mu = 176$. To achieve this contrast the value of μ_o is changed while the value of μ_d is held fixed at the value given in Table II. The results of this series are summarized in Fig. 12.

For $\Delta\mu = 0$ the electrostatic interactions are irrelevant to the energetics. A single hemispherical domain exists, as indicated by the linear correlation function crossing the line $C(r) = P$ at $r \approx 45$ nm. As $\Delta\mu$ increases, the correlation function abruptly shifts from linear to an exponential decay curve. This indicates that the hemispherical domain has dispersed into smaller irregular clusters. For dipole density contrast greater than $\Delta\mu = 130\ e^-/\mu$m correlation lengths range from 10 to 20 nm (inset of Fig. 12), consistent with the estimated size of nanodomains.

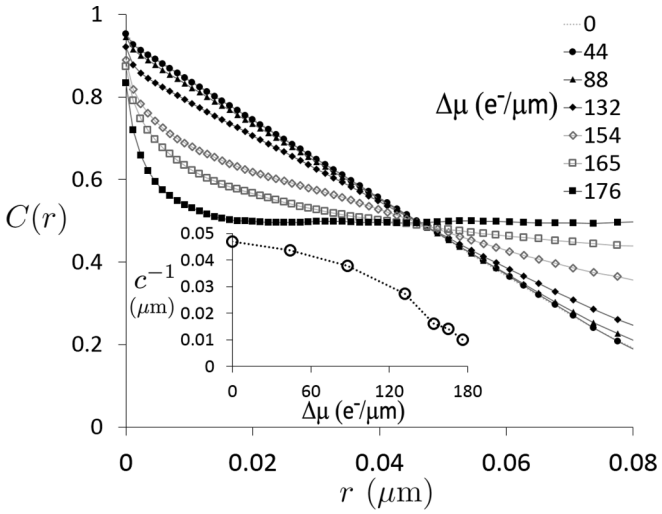

FIG. 12. Correlation functions for a series of dipole density contrasts $\Delta\mu$. As dipole contrast is increased the macroscopic domain morphology (straight line) abruptly transitions to an exponential decay. The inset shows the correlation length as a function of $\Delta\mu$.

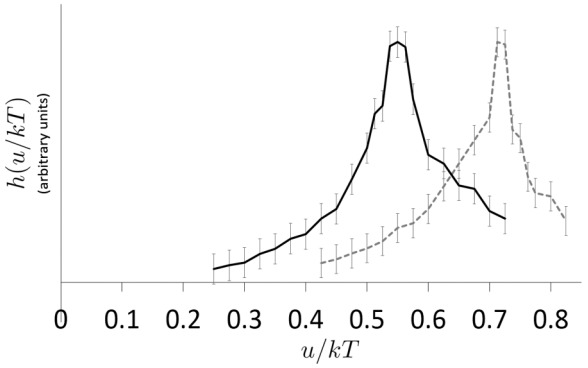

FIG. 13. Heat capacity for a spherical lattice without (black line) and with electrostatic repulsion (gray dashed line, with the parameters in Table I). Electrostatics shifts the critical point to the right, explaining why increasing dipole contrast can lead to an abrupt shift between macrodomains and nanodomains.

3. *Inclusion of dipoles shifts critical line tension to a higher value*

To better understand the mechanism behind the transition from macroscopic to nanoscopic phase separation caused by dipolar repulsion, we measure how the miscibility critical point has shifted. The heat capacity is measured as a function of u/kT for a dipole density contrast of $\Delta\mu = 176\ e^{-}/\mu$m and decay length of $k^{-1} = 2$ nm. The results of this calculation are shown in Fig. 13.

The inclusion of a dipolar repulsion term shifts the miscibility critical point to a higher value of u/kT than that of the triangular lattice Ising model. The critical point now occurs at $u_{\text{crit}}/kT \approx 0.72$. Once the dipole density contrast is high enough to shift the critical point above the current line tension ($u/kT = 0.7$) the system transitions from two coexisting phases to one phase. This shows why the transition observed when $\Delta\mu$ is increased occurs so abruptly. This finding is interesting; it shows a sharp transition from macroscopic to nanoscopic phase separation that is sensitive to a specific aspect of membrane composition. The local composition of the plasma membrane is known to be under tight regulation by the cell, thus providing a possible mechanism for the formation and dissipation of membrane rafts.

4. *Decay length of electric fields influences domain size*

The other parameter important for describing dipolar repulsion in the membrane is the decay length of the fields within the plane of the bilayer k^{-1}. Whereas the contrast $\Delta\mu$ describes the magnitude of the electric fields, the decay length describes how many shells of lipid are affected by the dipole moment of a given lipid. With the geometry of the bilayer fixed, the only external factor governing the decay length is the concentration and type of ions in the surrounding medium. For physiological conditions this decay length is 1.5–2 nm [24]. To explore how the decay length (and by extension the salt concentration) affects the phase morphology we performed a series of simulations, varying the decay length from $k^{-1} = 1$nm (high salt concentration) up to $k^{-1} = 3$ nm (low salt concentration). The resultant correlations functions are summarized in Fig. 14.

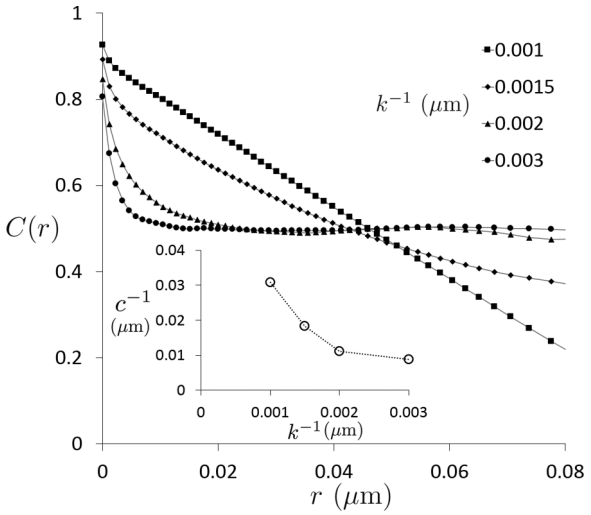

FIG. 14. Correlation functions for a series of decay lengths from $k^{-1} = 1$ to $k^{-1} = 3$ nm. The smallest decay length leads to macroscopic phase separation, which transitions smoothly to small clusters as k^{-1} is increased. The inset shows the correlation length as a function of k^{-1}, which shows that for $k^{-1} > 1.5$ nm, correlation lengths are on the order of 10 nm.

We find that as the decay length is increased the phase morphology shifts from macroscopic domains to clusters with progressively shorter correlation length (inset of Fig. 14). For the shortest decay length $k^{-1} = 1$ nm, the electric fields only extend roughly two lipid shells. Such a short decay length limits dipolar repulsion to a local effect that does not disrupt large-scale phase separation, as indicated by the linear correlation function.

As the decay length is extended, dipolar repulsion affects more and more shells of the lipid. The overlap in the electric fields from nearby lipids becomes more significant and frustrates the formation of a single large domain. This decrease in stability becomes apparent as the correlation function peels away from the macroscopic case and takes on the characteristic shape for irregular clusters.

The range of values examined here effectively covers the range of physically realizable decay lengths. The shorter decay lengths of 1–2 nm are expected for physiological conditions on the cytosolic side of the plasma membrane. The larger decay lengths greater than or equal to 3 nm are typical of conditions in GUV experiments, where sucrose-glucose solutions are used to provide density and optical contrast.

5. *Curvature and electrostatics stabilize circular domains on LUVs*

In our previous study of competing interactions and phase morphology [18], curvature was used as a competing interaction with line tension to break up macroscopic domains and stabilize modulated phases at an optical scale. Here we have shown that electrostatic repulsion is another interaction that can compete with line tension to produce phase morphology at nanodomain size scales. The next step in complexity for this model is to consider both electrostatics and curvature terms working in tandem and assess how the phase morphology is affected.

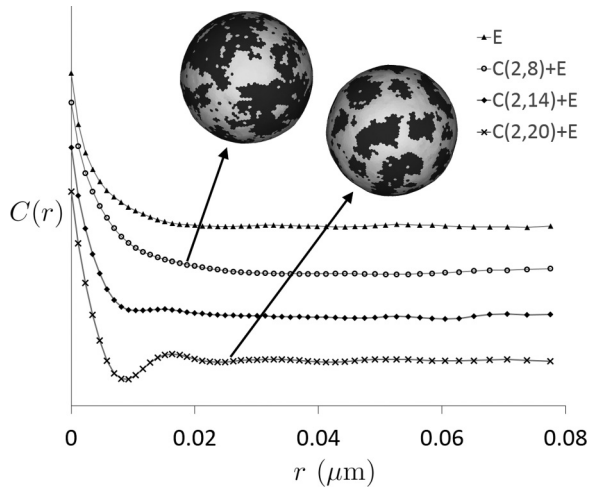

FIG. 15. Curvature and electrostatics together stabilize modulated phases on LUVs. With modest values of bending moduli, curvature alone (not shown) yields macroscopic phase separation, while electrostatics alone (E) yields a roughly 9-nm correlation length. Curvature with electrostatics $[C(\kappa_d,\kappa_o)+E]$ yields a slight increase in correlation length, followed by the formation of modulated phases with domain diameter of 8 nm as κ_o is increased. Correlation curves shown are stacked with a constant vertical offset.

The simulations in this section use the energy functional defined by Eq. (6) but also include the Helfrich curvature energy terms from Eq. (1). As a starting point for our exploration, bending modulus values are chosen similar to those measured by Semrau *et al.* [45] ($\kappa_d = 2\times10^{-19}$ J, $\kappa_o = [8-20]\times10^{-19}$ J) and the remaining parameters from Table II. A series of simulations was performed for increasing value of κ_o (and by extension $\bar{\kappa}_o$). The results of these simulations are shown in Fig. 15.

When electrostatic terms are not included these curvature parameters alone were not sufficient to disperse a macroscopic domain (not shown). By contrast, electrostatics alone (E) strongly opposed the formation of a single macroscopic domain, producing a correlation length of about 9 nm. When curvature is included together with electrostatics $[C(\kappa_d,\kappa_o)+E]$, the simulated domains become *larger*, e.g., the correlation length increases from 9 to 12 nm. This surprising result shows that curvature is not simply an interaction that opposes line tension, but instead works in a direction to minimize the frustration of bending the membrane. As κ_o is increased further, *modulated* phases precipitate with a *smaller* characteristic size of approximately 8 nm in diameter. Experimentally measured bending moduli already contain contributions from the dipole repulsion of nearby lipids, so we must be mindful of this when interpreting the values used to produce modulated phases in Fig. 15.

6. Comparison to SANS experiments

Recently the work of Heberle *et al.* [12] has shown that SANS experiments detect signatures of small domains on the surface of 60-nm LUVs. These measurements revealed domains approximately 14 nm in diameter in the model membrane system DSPC-POPC-chol.

With simulation parameters chosen to emulate these experimental conditions, we make a direct comparison of the length scales of our simulated morphology with those measured by neutron scattering. For electrostatic decay length of $k^{-1} = 3$ nm (no salt) and vesicle diameter of 60 nm the simulated phase domains have a correlation length of 9–11 nm (inset of Fig. 14). This result is close to the direct size measurements of SANS, showing that electrostatic repulsion can compete with line tension to stabilize structures in the predicted size range of the nanodomains.

IV. CONCLUSION

Expanding on the simulation techniques from our previous work [18], we have identified line tension as a running coupling constant, which necessitates the use of renormalization group techniques to properly account for how line tension must change as degrees of freedom are lost in coarse graining. The renormalization procedure we outline can be used to relate the line tension at any two grain levels to produce equivalent morphologies (defined as having the same correlation length). Furthermore, this technique may be used as a general way of empirically determining renormalization flows for a given parameter.

Background curvature is found to play an important role in the formation of modulated phases. When parameters that give modulated phases on a sphere are used on a flat sheet (of equivalent area and vertex density) modulated phases do not appear. A series of simulations in which background curvature was varied shows the transition to modulated phases only after a significant degree of background curvature is present.

We implement a model for the dipolar interactions between lipids and find that electrostatic repulsion can explain the formation of nanodomains in model membrane systems. Increasing the dipole density contrast $\Delta\mu$ leads to the breakup of macroscopic domains into irregular clusters. The nature of this transition is caused by a shift of the miscibility critical point to a higher value of line tension.

The decay length of the electric fields within the plane of the bilayer is found to be important to the phase morphology. Even though electrostatic interactions have a decay length of only a few nanometers, this is still several lipid shells, which proves important at the small scales relevant to nanodomains and membrane rafts. Varying the decay length from 1 nm up to 3 nm can drive a transition from macroscopic domains to clusters with correlation lengths on the order of 10 nm.

Surprisingly, on a highly curved membrane (such as the surface of 60-nm vesicles) the inclusion of both curvature and electrostatics can lead to a larger overall domain size than with electrostatic repulsion alone. This increase shows that curvature can work to either stabilize or disperse domains, depending on the parameters and interactions used in the simulation. Further increasing the stiffness of the raft phase leads to the formation of modulated phases. This result is surprising because all bending moduli used in this study produce only macroscopic phase separation in the absence of the electrostatic interaction.

The size of simulated domains for 60-nm LUVs can be compared to the experimentally measured domain

sizes from SANS. The range of correlation lengths from simulations (9–11 nm) matched well with the measured domain size in the model system DSPC-POPC-chol (≈14 nm in diameter). Thus a dipolar repulsion can compete with line tension to stabilize phase domains on the nanometer scale.

ACKNOWLEDGMENTS

Support was from NSF research Grant No. NSF MCB 0842839 (to G.W.F.). J.J.A. received support from NIH Training Grant No. 1-T32 GM 08267. We thank Professor Benjamin Widom for help in formulating our ideas about renormalization and scaling.

[1] M. Swamy, L. Ciani, M. Ge, A. Smith, D. Holowka, B. Baird, and J. Freed, Biophys. J. **90**, 4452 (2006).
[2] P. Sengupta, D. Holowka, and B. Baird, Biophys. J. **92**, 3564 (2007).
[3] S. Munro, Cell **115**, 377 (2003).
[4] D. Lingwood and K. Simons, Science **327**, 46 (2010).
[5] M. Ediden, Nat. Rev. **4**, 414 (2003).
[6] I. Levental, M. Grzybek, and K. Simons, Proc. Natl. Acad. Sci. USA **108**, 11411 (2011).
[7] K. Simons and G. van Meer, Biochemistry **27**, 6197 (1988).
[8] L. Pike, J. Lipid Res. **44**, 655 (2003).
[9] J. Zhao, J. Wu, F. Heberle, T. Mills, P. Klawitter, G. Huang, G. Costanza, and G. Feigenson, Biochim. Biophys. Acta **1768**, 2764 (2007).
[10] A. Ayuyan and F. Cohen, Biophys. J. **94**, 2654 (2008).
[11] F. Heberle, J. Wu, S. Goh, R. Petruzielo, and G. Feigenson, Biophys. J. **99**, 3309 (2010).
[12] F. Heberle, R. Petruzielo, J. Pan, P. Drazba, N. Kucerka, R. Standaert, G. Feigenson, and J. Katsaras, J. Am. Chem. Soc. **135**, 6853 (2013).
[13] G. Feigenson and J. Buboltz, Biophys. J. **80**, 2775 (2001).
[14] D. Brown, Physiology **21**, 430 (2006).
[15] K. Simons and W. Vaz, Annu. Rev. Biophys. Biomol. Struct. **33**, 269 (2004).
[16] S. Goh, J. Amazon, and G. Feigenson, Biophys. J. **104**, 853 (2013).
[17] T. Konyakhina, S. Goh, J. Amazon, F. Heberle, J. Wu, and G. Feigenson, Biophys. J. **101**, L08 (2011).
[18] J. J. Amazon, S. L. Goh, and G. W. Feigenson, Phys. Rev. E **87**, 022708 (2013).
[19] M. Seul and D. Andelman, Science **267**, 476 (1995).
[20] T. Kawakatsu, D. Andelman, K. Kawasaki, and T. Taniguchi, J. Phys. II France **3**, 971 (1993).
[21] A. Imperio and L. Reatto, J. Chem. Phys. **124**, 164712 (2006).
[22] J. Hu, T. Weikl, and R. Lipowsky, Soft Matter **7**, 6092 (2011).
[23] W. Helfrich and R. Servuss, Nuovo Cimento **3**, 137 (1984).
[24] See Supplemental Material at http://link.aps.org/supplemental/10.1103/PhysRevE.89.022702 for proof of the edge-case Guassian curvature equation and a detailed explanation of decay length calculations.
[25] A. Travesset, J. Chem. Phys. **125**, 084905 (2006).
[26] J. T. Groves, Annu. Rev. Phys. Chem. **58**, 697 (2007).
[27] J. Liu, S. Qi, J. Groves, and A. Chakraborty, J. Phys. Chem. B **109**, 19960 (2005).
[28] S. Duane and R. Horgan, Z. Phys. C **16**, 355 (1983).
[29] H. Kleinert, Phys. Lett. A **114**, 263 (1986).
[30] R. Houtappel, Physica **16**, 425 (1950).
[31] A. Honerkamp-Smith, P. Cicuta, M. Collins, S. Veatch, M. Nijs, M. Schick, and S. Keller, Biophys. J. **95**, 236 (2008).
[32] B. Machta, S. Papanikolau, J. Sethna, and S. Veatch, Biophys. J. **100**, 1668 (2011).
[33] D. Marsh, Chem. Phys. Lipids **144**, 146 (2006).
[34] M. Hu, J. Briguglio, and M. Deserno, Biophys. J. **102**, 1403 (2012).
[35] T. Ursell, W. Klug, and R. Phillips, Proc. Natl. Acad. Sci. USA **106**, 13301 (2009).
[36] I. Parmryd and B. Onfelt, FEBS J. **280**, 2775 (2013).
[37] S. Veatch and S. Keller, Biochim. Biophys. Acta **1746**, 172 (2005).
[38] L. Wang, Annu. Rev. Biochem. **81**, 615 (2012).
[39] L. Wang, P. Bose, and F. Sigworth, Proc. Natl. Acad. Sci. USA **103**, 18528 (2006).
[40] A. Smondyrev and M. Berkowitz, Biophys. J. **78**, 1672 (2000).
[41] H. Nymeyer and H. Zhou, Biophys. J. **94**, 1185 (2008).
[42] A. Raudino and D. Mauzerall, Biophys. J. **50**, 441 (1986).
[43] U. Peterson, D. Mannock, R. Lewis, P. Pohl, R. McElhaney, and E. Pohl, Chem. Phys. Lipids **117**, 19 (2002).
[44] A. Demchenko and S. Yesylevskyy, Chem. Phys. Lipids **160**, 63 (2009).
[45] S. Semrau, T. Idema, L. Holtzer, T. Schmidt, and C. Storm, Phys. Rev. Lett. **100**, 088101 (2008).